Direct Evidence for Coupled Surface and Concentration Quenching Dynamics in Lanthanide-Doped Nanocrystals

Noah J. J. Johnson,[†,⊥] Sha He,[‡,⊥] Shuo Diao,[§] Emory M. Chan,[∥] Hongjie Dai,[§] and Adah Almutairi*,[†,‡]

[†]Skaggs School of Pharmacy and Pharmaceutical Sciences and [‡]Department of NanoEngineering, University of California, San Diego, 9500 Gilman Drive, La Jolla, California 92093, United States

[§]Department of Chemistry, Stanford University, Stanford, California 94305, United States

[∥]The Molecular Foundry, Lawrence Berkeley National Laboratory, Berkeley, California 94720, United States

S *Supporting Information*

ABSTRACT: Luminescence quenching at high dopant concentrations generally limits the dopant concentration to less than 1−5 mol% in lanthanide-doped materials, and this remains a major obstacle in designing materials with enhanced efficiency/brightness. In this work, we provide direct evidence that the major quenching process at high dopant concentrations is the energy migration to the surface (i.e., surface quenching) as opposed to the common misconception of cross-relaxation between dopant ions. We show that after an inert epitaxial shell growth, erbium (Er^{3+}) concentrations as high as 100 mol% in $NaY(Er)F_4/NaLuF_4$ core/shell nanocrystals enhance the emission intensity of both upconversion and downshifted luminescence across different excitation wavelengths (980, 800, and 658 nm), with negligible concentration quenching effects. Our results highlight the strong coupling of concentration and surface quenching effects in colloidal lanthanide-doped nanocrystals, and that inert epitaxial shell growth can overcome concentration quenching. These fundamental insights into the photophysical processes in heavily doped nanocrystals will give rise to enhanced properties not previously thought possible with compositions optimized in bulk.
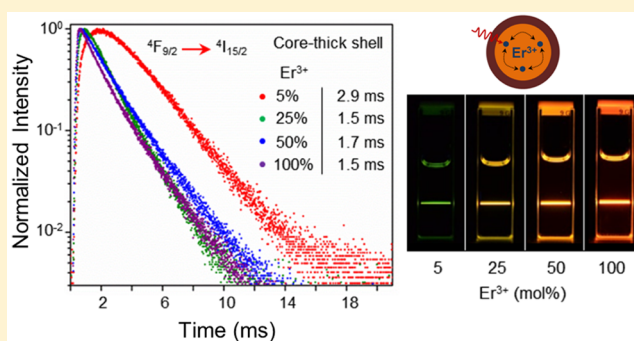
■ INTRODUCTION

Lanthanide-doped nanocrystals have generated significant interest for a broad range of applications from bioimaging and photovoltaics to displays.[1−4] Using selective combinations/compositions of lanthanide dopants, various photophysical processes such as quantum cutting, downshifting, and upconversion can be realized in this class of materials.[5−10] Common limitations for realizing practical applications are the limited brightness of lanthanide-doped nanocrystals and the challenges associated with enhancing luminescence efficiencies. One critical limitation of lanthanide-doped nanocrystals is that the concentration of dopants (emitter ion) is generally restricted to 1−5 mol%. Increasing the dopant concentration results in decreasing luminescence intensity, commonly referred to as "concentration quenching". Despite the fact that the origins of concentration quenching in lanthanide-doped materials are still under debate,[7] these guidelines and the optimized concentrations from bulk materials are commonly adopted in lanthanide-doped nanocrystals.[11,12] Only recently, efforts to achieve high dopant concentrations are being addressed especially in lanthanide-doped upconversion nanocrystals. Zhao et al.[13,14] and Gargas et al.[15] independently demonstrated the use of high excitation irradiance (~10^6 W cm$^{−2}$) as a way to overcome concentration quenching at high dopant concentrations. Similarly, Liu and co-workers demon-

strated the sublattice clustering of dopant ions as a pathway to achieve high dopant concentrations.[16] More recently, Prasad and co-workers used organic dye sensitization as a route to alleviate concentration quenching.[17] However, mechanistic investigations to understand the origins of concentration quenching and ways to overcome them especially with nanocrystalline materials are not fully addressed.

Two common explanations for concentration quenching are deleterious cross-relaxation between dopant ions in close proximity,[13] and/or enhanced energy migration via resonant energy transfer to the defects (i.e., the surface).[12] While the latter has only gained attention in the past decade with the development of colloidal nanocrystals, historically the cross-relaxation between dopant ions is commonly regarded as the major cause of concentration quenching as observed in bulk materials. In this work, we address this fundamental question on the origins of concentration quenching in nanocrystalline materials, and demonstrate that the major quenching process at high dopant concentrations is predominantly due to energy migration to the surface and not cross-relaxation between dopant ions.
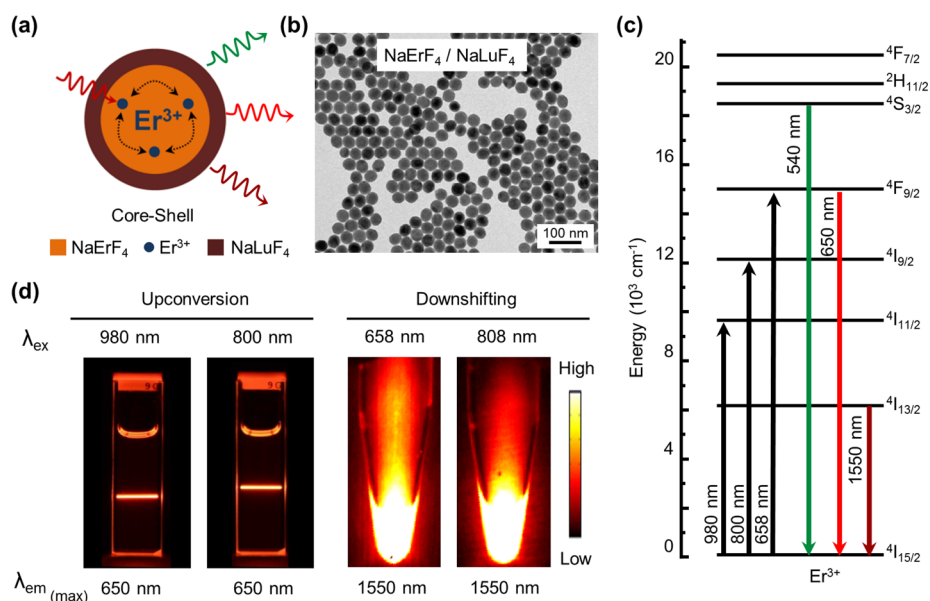
Figure 1. (a) Schematic illustration of the core−shell nanocrystals structural composition. (b) Representative transmission electron microscopy (TEM) image of the $NaErF_4$−$NaLuF_4$ core−shell nanocrystals. (c) Energy level diagram of erbium showing the multiple excitation pathways, and the multiple emission levels leading to upconverted or downshifted emission. (d) Upconversion and downshifted emission photographs of the colloidal dispersion of $NaErF_4$−$NaLuF_4$ core−shell nanocrystals at variable excitation wavelengths.
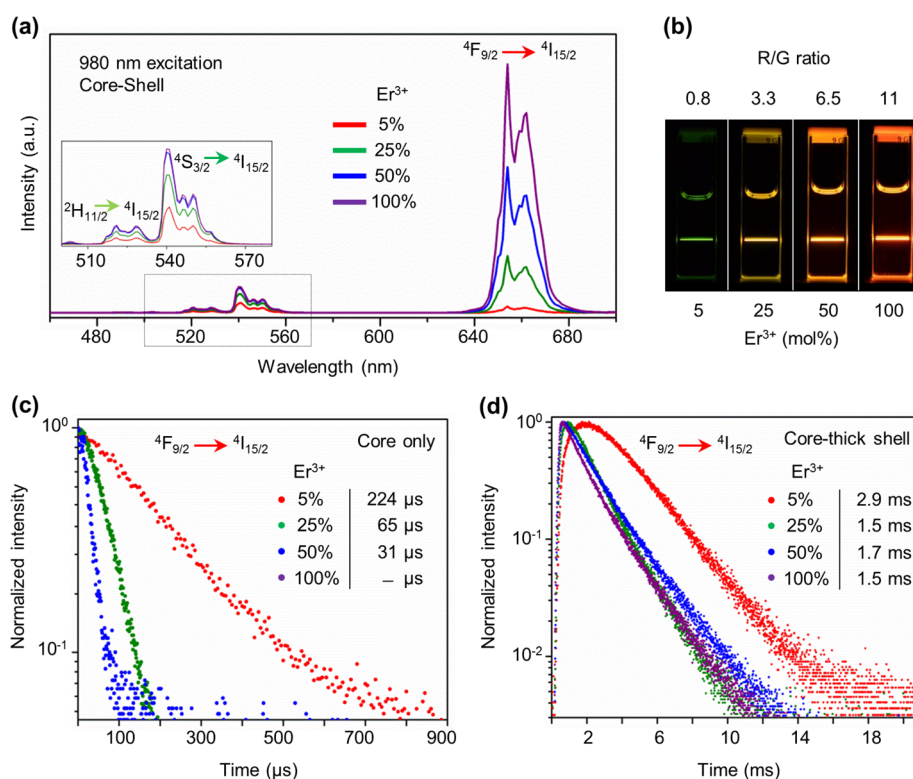

Figure 2. (a) Upconversion emission spectra of the core−shell nanocrystals with variable Er^{3+} dopant concentrations in the core ($NaYF_4$:X mol% Er^{3+}, X = 5, 25, 50, and 100 mol%), Inset shows the green emission bands. (b) Upconversion emission photos of colloidal dispersion of core−shell nanocrystals (λ_{exc} = 980 nm), showing the enhanced emission with increase in dopant concentration. Luminescence decay of the $^4F_{9/2}$ level at 650 nm with variable erbium dopant concentration and their corresponding lifetime values of the (c) core nanocrystals and (d) core−shell nanocrystals.

In colloidal nanocrystals, increasing the dopant ion concentration results in increased energy migration to the surface as the interionic distance shortens.[18] This suggests that the concentration quenching effects should be strongly coupled to the surface effects in nanocrystalline materials. In lanthanide-doped nanocrystals, the emission intensity decreases dispro-portionately with nanocrystal volume due to the fact that a significant fraction of the dopants lie within the characteristic distance for energy migration.[19−21] Recent advances have established that the epitaxial growth of a shell spatially isolates the core, passivates surface defects, and reduces surface quenching.[22−31] In this context, we reasoned that the growth

of thick (~10 nm) high-quality epitaxial shell should decouple both the surface and concentration quenching effects and allow for higher dopant concentrations within the core than those optimized in bulk compositions. Moreover, the ability to localize high dopant concentration in the core and confine the excitation energy with a high-quality shell should allow for novel mechanistic understanding of the photophysical processes that have not been previously possible with bulk materials or core only nanostructures.

RESULTS AND DISCUSSION

In this work, erbium (Er^{3+}) is used as the active dopant ion for its rich energy level system that offers multiple excitation and emission pathways spanning the visible to the near-infrared (NIR) wavelengths. To systematically study and compare the effect of epitaxial shells on heavily doped nanocrystals, we synthesized hexagonal phase (β) $NaYF_4$ core NCs with varying Er^{3+} dopant concentrations (5, 25, 50, and 100 mol%),[32] followed by growing an inert thick (~10 nm) $NaLuF_4$ epitaxial shell (see experimental details for synthesis).[24,33] All core NCs were similar in size (~15 nm), and after shell growth the core–shell NCs were found to be about ~35–38 nm, with an average shell thickness of about 10 nm as shown in Figures S1 and S2, respectively. A schematic representation of the core–shell structure and transmission electron microscopy (TEM) image of 100 mol% Er-doped $NaYF_4$ core (i.e., $NaErF_4$) with a $NaLuF_4$ shell is shown in Figure 1a,b, respectively. Representative scanning electron microscopy (SEM), high resolution (HR)-TEM, and powder X-ray diffraction (XRD) analysis shown in Figures S3 and S4 further confirmed the high uniformity, crystallinity, and hexagonal phase of the synthesized core–shell nanocrystals. Upconversion and downshifted luminescence at various excitation fluxes for the erbium dopants as shown in the energy level diagram (Figure 1c) were systematically investigated for these doped core and core–shell nanostructures. Figure 1d shows the dispersion photographs of the same dispersion of core-thick shell nanocrystals at variable excitation fluxes and emission pathways studied in this work.

We first investigated the upconversion emission properties of the core nanocrystals under 980 nm continuous-wave (CW) diode laser excitation. Consistent with concentration quenching the upconversion emission intensity decreases with increasing erbium concentration in the core nanocrystals (Figure S5). The visible green ($^2H_{11/2} \rightarrow {}^4I_{15/2}$ and $^4S_{3/2} \rightarrow {}^4I_{15/2}$), and red ($^4F_{9/2} \rightarrow {}^4I_{15/2}$) emission bands are strongest for the 5 mol% Er^{3+}-doped nanocrystals, and decrease with increasing erbium concentration, while being completely quenched in the heavily doped (100 mol% Er^{3+} or $NaErF_4$) nanocrystals. Surprisingly, after a thick (~10 nm) $NaLuF_4$ epitaxial shell growth on these nanocrystals we find that the upconversion emission increases monotonically with increasing erbium concentration, with the brightest being the heavily doped (100 mol% Er^{3+}) nanocrystals (Figure 2a). The enhanced upconverted emission with increase in dopant concentration is observed clearly in the digital photographs of the colloidal dispersion of the core–shell NCs (λ_{exc} = 980 nm) shown in Figure 2b. The enhanced luminescence from the 100 mol% Er^{3+}-doped ($NaErF_4$–$NaLuF_4$) core–shell nanocrystals from a completely quenched core only structure ($NaErF_4$), establishes that surface quenching and concentration quenching are strongly coupled, and highlights the role of epitaxial shell in decoupling these effects. Note that we do not provide an enhancement factor for

the brightest core–shell structure, as the core is completely quenched with no observable/measurable emission.

Since concentration and surface quenching would decrease the lifetime of emitting states, we examined the time-resolved population of the red emitting ($^4F_{9/2}$) level under 980 nm excitation for the core and core–shell nanocrystals. For the core nanocrystals, the luminescence lifetime decreased from 224 to 31 μs as the dopant concentration increased from 5 to 50 mol% (Figure 2c, with full lifetime curves in Figure S5), and was completely quenched for the 100 mol% core nanocrystals. This concentration dependence in lifetime is consistent with the increased probability of energy migrating to the surface as the dopant concentration increases and the interionic distance shortens.[12] However, these measurements do not exclude cross-relaxation as a mechanism for concentration quenching, since cross-relaxation would also reduce the luminescence lifetimes at high emitter concentrations. To distinguish between the two mechanisms, we measured the lifetimes of the thick-shell nanocrystals, thereby eliminating energy migration to the surface. In contrast to the sharp concentration dependence and μs lifetimes of the cores, all of the core–shell nanocrystals exhibit long luminescence lifetimes greater than 1 ms with surprisingly little dependence on concentration (Figure 2d). While the lifetime increased from 224 μs to 2.9 ms for the 5 mol% Er^{3+}-doped nanocrystals after shell growth, the 100 mol% Er^{3+}-doped nanocrystals increased from a completely quenched (dark) state to 1.5 ms after shell growth. The similar decay time of ~1.5 ms for the 25, 50, and 100 mol% Er^{3+}-doped samples after shell growth, demonstrates that, even under high dopant concentrations that in principle favor rapid cross relaxation, no "concentration quenching" is observed in the lifetime or the emission of core–shell nanocrystals. This suggests that cross-relaxation is not the dominant mechanism for concentration quenching. In contrast, when energy migration to the surface is suppressed by the growth of a thick shell, the heavy "concentration quenching" observed with the original cores is deactivated. These dual observations lead to the conclusion that energy migration to surface defects, not cross-relaxation is the major luminescence quenching pathway at high dopant concentrations.

Similar behavior is observed for the time-resolved population of the green emitting level ($^4S_{3/2} \rightarrow {}^4I_{15/2}$) under 980 nm excitation (Figure S6). As expected the lifetime values of this level ($^4S_{3/2}$) were slightly shorter than the strongly red-emitting level ($^4F_{9/2}$).[34] Remarkably, for the brightest heavily doped (100 mol% Er^{3+}) core–shell nanocrystal, we determined the upconversion quantum yield under 980 nm excitation to be 5.2 ± 0.3% at only 10 W cm^{-2} irradiance (see materials and methods section for details). This further confirms the unique ability of epitaxial shell in overcoming concentration quenching, providing access to the benefits of high-dopant concentrations (i.e., more emission centers) without the disadvantages of quenching in high-surface-area nanocrystalline structures.

To demonstrate the generality of this unique observation, we explored the upconversion emission properties of these core–shell nanocrystals under a second excitation wavelength. The transition from erbium ground state ($^4I_{15/2}$) to the $^4I_{9/2}$ manifold (Figure 1c) allows for direct excitation of the erbium at 800 nm, which lies in the NIR-I bioimaging window. Recent interest in excitation energy tuning in upconversion nanocrystals, especially using neodymium (Nd^{3+}) sensitization has focused on 800 nm excitation, for its biocompatibility, and minimal heating effects as compared to the conventional 980
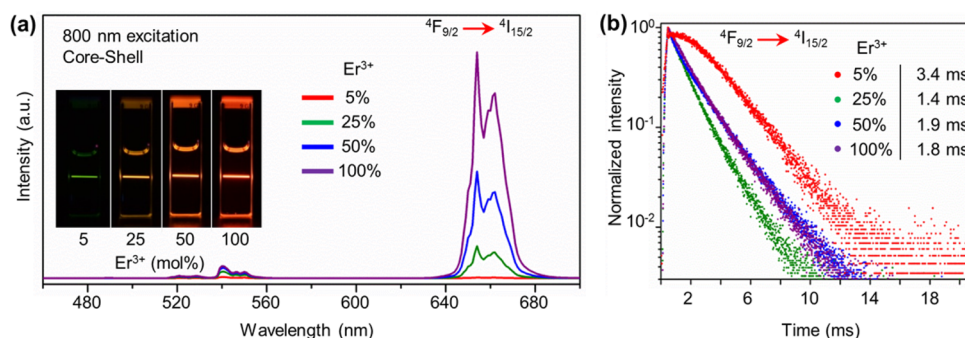
Figure 3. (a) Upconversion spectra of the core−shell nanocrystals with variable Er^{3+} dopant concentrations in the core ($NaYF_4$:X mol% Er^{3+}, X = 5, 25, 50, and 100 mol%). Inset shows the upconversion emission photos of colloidal dispersion of core−shell nanocrystals showing the enhanced emission with increase in dopant concentration. (b) Luminescence decay of the $^4F_{9/2}$ level at 650 nm of the core−shell nanocrystals with variable erbium dopant concentration and their corresponding lifetime values.

nm excitation.[30,35] Here, too, we observe a strong upconversion enhancement with increasing Er^{3+} dopant concentration in the core−shell nanocrystals, with the brightest being the heavily doped (100 mol% Er^{3+}) core with a thick (~10 nm) $NaLuF_4$ shell (Figure 3a). Similar to the 980 nm excitation, the upconversion showed stronger monotonic enhancement of the red emission band with increasing dopant concentration (see inset Figure 3a for digital photographs of the upconversion emission). The luminescence decay curves of the red emitting level ($^4F_{9/2} \rightarrow {}^4I_{15/2}$) upon 800 nm excitation shown in Figure 3b, once again exhibit long lifetimes that are independent of dopant concentration at high Er^{3+} concentrations (25, 50, and 100 mol%), confirming the generality of our observations (Figure 3b). The enhanced upconverted emission observed at two separate excitation wavelengths from a core nanocrystal (100 mol% Er^{3+}) that is completely quenched, demonstrate the unique potential of the epitaxial shell in overcoming concentration quenching. Note that the epitaxial shells grown here are isotropic to the core, providing high-quality spatial confinement of the core from surface effects.

Next, we reasoned that suppression of both concentration and surface quenching in core−shell structures could also enhance the emission of Stokes, or downshifted emission in heavily doped nanocrystals. Er^{3+}-doped nanocrystals emit NIR light centered at 1550 nm via radiative relaxation from the first Er^{3+} excited state ($^4I_{13/2}$) to the ground state ($^4I_{15/2}$) (Figure 1c). This emission band lies within the NIR-II biological window (1000−1700 nm) that is currently being explored for bioimaging,[36] as it offers reduced tissue scattering and autofluorescence.[37,38] Moreover, this emission band has critical importance for optical amplifiers as it overlaps with the minimal loss window (telecommunication window) in silica fibers.[39] However, due to concentration quenching, studies to date have been limited to erbium dopant concentrations below 2−5 mol %.[12,40] We first investigated the downshifted NIR emission (1550 nm) from the core−shell nanocrystals excited at 808 nm ($^4I_{15/2} \rightarrow {}^4I_{9/2}$) (see Figure 4a for energy level diagram). The emission intensity at 1550 nm exhibited a strong enhancement with increasing Er^{3+} dopant concentration (Figure 4b), with the heavily doped (100 mol% Er^{3+}) core−shell nanocrystals as the brightest. The NIR emission images of the colloidal dispersion of core−shell nanocrystals (Figure 4c) excited at 808 nm clearly illustrate the enhanced emission at high dopant concentrations, demonstrating the ability of epitaxial shell to enhance the downshifted emission from heavily doped nanocrystals. Similar enhancement of downshifted NIR emission (1550 nm) with
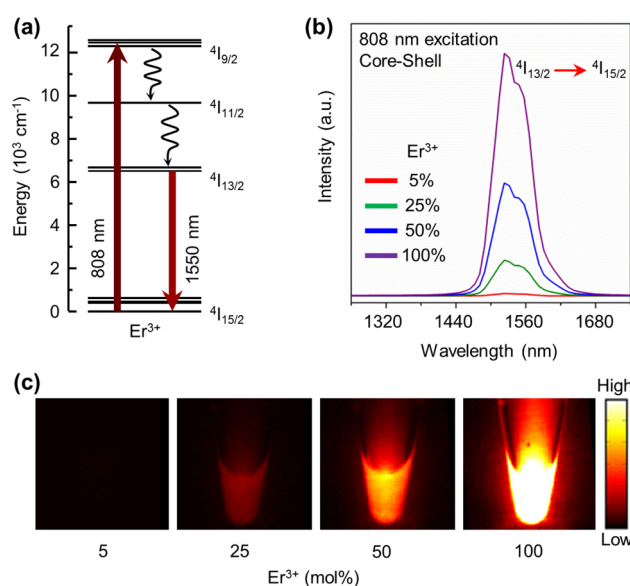

Figure 4. (a) Energy level diagram of Er^{3+} showing the excitation (808 nm) and the downshifted emission (1550 nm) levels. (b) Emission spectra of the core−shell nanocrystals with variable Er^{3+} dopant concentrations in the core showing downshifted infrared emission between 1450 and 1650 nm under 808 nm excitation. (c) Downshifted emission images from colloidal dispersion of core−shell nanocrystals (λ_{exc} = 808 nm) in the range of 0.9−1.7 μm, showing emission enhancement with increase in dopant concentration.

increase in dopant concentration is also observed on excitation at 658 nm ($^4I_{15/2} \rightarrow {}^4F_{9/2}$), and we again find the heavily doped core−shell (100 mol% Er^{3+} in core) to be the brightest (Figure S7). These results provide direct evidence of achieving enhanced emission from a lanthanide-doped structure with a high active dopant concentration reaching 100 mol%, and establish the unique role of inert epitaxial thick shell.

To validate the role of the inert/undoped shell in suppressing surface and concentration quenching, we attempted to reactivate energy migration pathways by modulating the shell thickness, and by introducing dopants into the shell using the 100 mol% Er^{3+}-doped nanocrystals ($NaErF_4$) as core. First, core−shell nanocrystals with an undoped/inert $NaLuF_4$ shell having variable shell thickness ($d \approx 2.5$, 5, and 8 nm) were synthesized (see Figure S8, and experimental details for synthesis). In 100 mol% Er^{3+} core nanocrystals, all of the erbium centers are effectively coupled to the surface,

completely quenching the upconverted luminescence at 980 nm excitation (Figure 5a,b, d = 0 nm). After shell growth, we
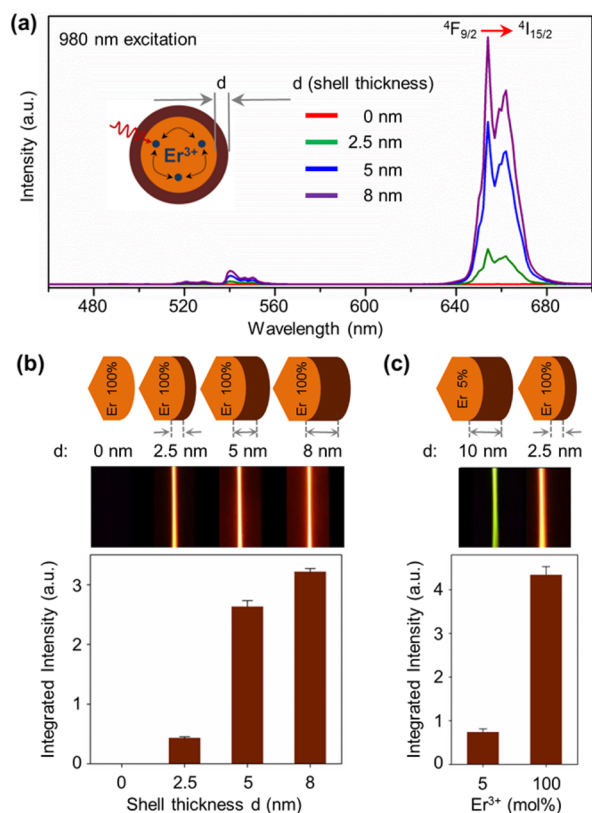

Figure 5. (a) Upconversion emission spectra of $NaErF_4$ core (d = 0 nm), and $NaErF_4$–$NaLuF_4$ core–shell nanocrystals with increasing shell thickness, λ_{exc} = 980 nm. (b) Integrated emission intensity as a function of shell thickness, and upconversion emission photos of colloidal dispersion of core–shell nanocrystals as a function of shell thickness. (c) Normalized integrated emission intensity of $NaYF_4$:Er^{3+}(5 mol%)–$NaLuF_4$ core–shell nanocrystal with a shell thickness of d = 10 nm and $NaErF_4$–$NaLuF_4$ core–shell nanocrystal with a shell thickness of d = 2.5 nm, and the respective upconversion emission photos of the colloidal dispersion.

observe a consistent increase in upconversion emission intensity with increasing shell thickness (Figure 5a,b), illustrating that the epitaxial shell decouples the erbium centers coupled to the surface (Figure S9 shows upconversion directly from the core–shell reaction flask). The strong coupling of surface and concentration quenching processes with increase in dopant concentration in the core is clearly evident on comparing the 5 and 100 mol% Er^{3+}-doped core–shell nanocrystals with different shell thickness (Figure 5c). The emission intensity of the 100 mol% Er^{3+}-doped nanocrystals with a thin 2.5 nm shell is already 3 times higher than that of the 5 mol% Er^{3+}-doped nanocrystals with a thick 10 nm shell; note that as a core, 5 mol% doped nanocrystals are the brightest and 100 mol% doped nanocrystals are completely quenched (dark). Taken together, our findings highlight the striking interdependence of surface and concentration effects, and demonstrate the role of epitaxial shell in decoupling these effects to achieve enhanced photophysical properties from heavily doped nanostructures.

Finally, we hypothesized that if energy migration to the surface was the origin of concentration quenching, doping the

epitaxial shell would reactivate quenching pathways and quench the emission. Core–shell nanocrystals with variable ytterbium (Yb^{3+}) dopants concentrations (10 and 20 mol%) in the shell and 100 mol% Er^{3+} in the core, were used to study upconversion emission at 980 nm excitation (Figure S10). Doping ions in separate layers is a common strategy in conventional platforms to enhance the photophysical processes,[41] and to avoid deleterious cross-relaxation between the active emitter and sensitizer ions. The overlap of $^2F_{5/2}$ level of Yb^{3+} with $^4I_{11/2}$ level of Er^{3+} (Figure 6a) allows for sensitizing upconversion at 980 nm excitation. Yb^{3+} doping in the shell resulted in luminescence quenching with increasing dopant concentration (Figure 6b), resulting from the coupling of the core Er^{3+} ions to the surface through the Yb^{3+} centers in the shell. Similarly, doping neodymium (Nd^{3+}) in the shell quenched the upconversion emission under 800 nm excitation, even at very low (2 mol%) dopant concentration in the shell (Figure 6c,d). The reactivation of concentration quenching by introducing dopants in the shell and also by modulating the shell thickness further highlights the critical importance for an inert and thick epitaxial shell to overcome concentration quenching.

We have thus provided here four independent results that together offer definitive evidence that "concentration quenching" is inexorably coupled to and a consequence of energy migration to surface defects. The four points of evidence supporting this are (1) the concentration-dependent quenching of heavily doped cores, (2) the strong enhancement of intensity with shell growth, (3) the lack of concentration dependence of the excited state lifetimes in core–shell nanocrystals, and (4) the reactivation of concentration quenching by doping the shells/reducing the shell thickness. Taken together, these results provide a new fundamental insight on the excited state energy dynamics that is unique to core–shell nanostructures, and provide a unique pathway to achieve high dopant concentrations with negligible quenching effects that are not achievable in bulk or core only structures.

◼ CONCLUSIONS

In summary, our results provide new fundamental insights on energy migration, dopant concentration and surface effects in lanthanide-doped nanocrystals. First, the brightest core nanocrystals do not necessarily produce the brightest core–shell structures upon epitaxial growth, which is counterintuitive. In fact, the brightest core–shell structure is completely "dark" or quenched as a core-only structure, highlighting the strong coupling of surface/concentration effects in nanocrystalline materials. Second, the luminescence decay curves of the heavily doped core–shell nanocrystals unequivocally demonstrate that the major deactivation pathway at high dopant concentrations is the energy migration to the surface as opposed to cross-relaxation between neighboring ions. Third, the enhancement of multiple photophysical processes from heavily doped (100 mol%) core–shell nanocrystals demonstrated here clearly establishes that concentration quenching can be overcome with inert epitaxial shell growth. This unexplored regime of spatially confined heavily doped nanostructures establishes a new paradigm in modulating/enhancing the photophysical processes in lanthanide-doped structures, and open new opportunities toward exploring unique nanoscale compositions that do not necessarily depend on compositions previously optimized in bulk.
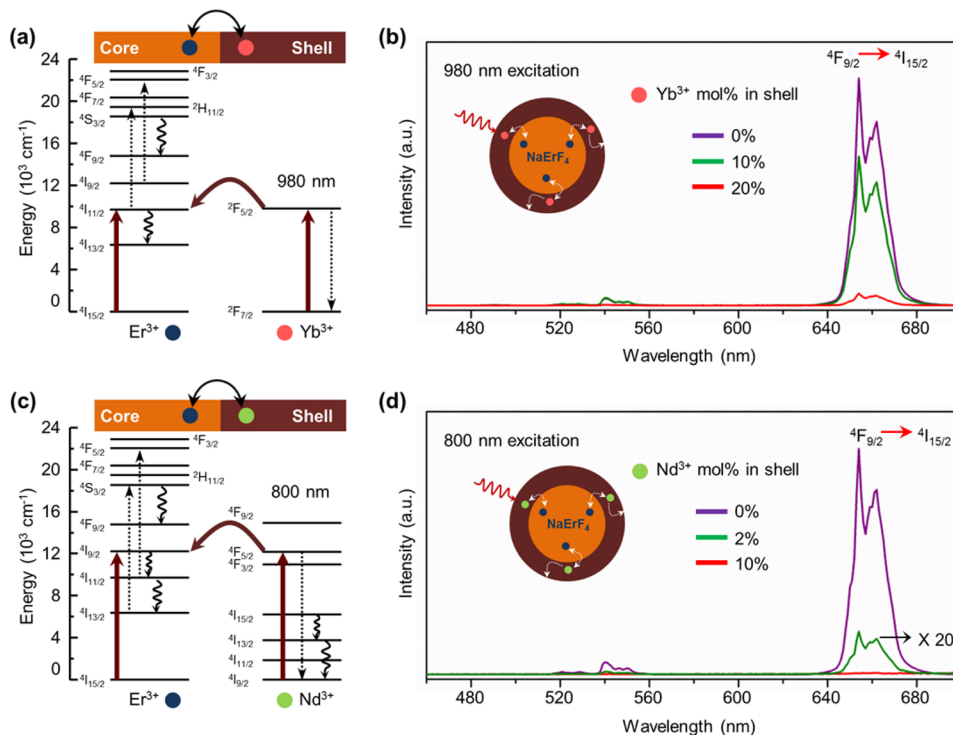
Figure 6. (a) Energy levels of core Er^{3+} and sensitizer Yb^{3+} in the shell showing possible energy transfer upon 980 nm excitation. (b) Upconversion emission spectra $NaErF_4-NaLuF_4$ core−shell nanocrystals with variable Yb^{3+} doping in the shell. (c) Energy levels of core Er^{3+} and sensitizer Nd^{3+} in the shell showing possible energy transfer upon 800 nm excitation. (d) Upconversion emission spectra $NaErF_4-NaLuF_4$ core−shell nanocrystals with variable Nd^{3+} doping in the shell.

■ MATERIALS AND METHODS

Chemicals. Yttrium(III) acetate hydrate (99.9%), erbium(III) acetate hydrate (99.9%), neodymium(III) oxide (99.9%), ytterbium-(III) oxide (99.9%), sodium trifluoroacetate (98%), oleic acid (90%), 1-octadecene (90%), and oleylamine (70%) were purchased from Sigma-Aldrich. Lutetium(III) oxide (99.9%) from Alfa Aesar, sodium hydroxide from Fisher Scientific, and ammonium fluoride from Spectrum. All chemicals were used as received.

Synthesis of Core Nanocrystals. Hexagonal phase (β) $NaYF_4$ (X mol% Er^{3+}) (X = 5, 25, 50)-doped nanocrystals were synthesized following a previously reported procedure with slight modifications from calculated amounts of $Y(CH_3CO_2)_3 \cdot xH_2O$ and $Er(CH_3CO_2)_3 \cdot xH_2O$ to a total of 1.0 mmol.[32] In a typical synthesis, acetate salts (1.0 mmol), oleic acid (6 mL), and 1-octadecene (17 mL) were taken in a 100 mL flask and heated to 120 °C under vacuum for 1 h and cooled to room temperature. To this solution at room temperature, a methanol solution (10 mL) of ammonium fluoride (4 mmol) and sodium hydroxide (2.5 mmol) was added and stirred for 1 h. The reaction vessel was then heated to 70 °C to remove methanol and subsequently heated to 300 °C (~10 °C/min) under argon and maintained for 60 min to obtain the erbium-doped core $NaYF_4$ nanocrystals. (The shell growth was then performed directly on the core nanocrystals using sacrificial nanocrystals; see Synthesis of Core−Shell Nanocrystals section below.) Hexagonal phase (β) $NaErF_4$ nanocrystals were synthesized as described for the (β) $NaYF_4$-doped nanocrystals, except that $Er(CH_3CO_2)_3 \cdot xH_2O$ (1.0 mmol), oleic acid (4.5 mL), and 1-octadecene (15 mL) were used.

Synthesis of Sacrificial Nanocrystals as Shell Precursors. Cubic (α) $NaLuF_4$ nanocrystals were synthesized based on a previously reported procedure with slight modifications.[33] In a typical synthesis Lu_2O_3 (1 mmol) was mixed with 20 mL of 50% aqueous trifluoroacetic acid and refluxed at 95 °C overnight to get a clear solution. The trifluoroacetate precursor ($Lu(CF_3COO)_3$) was then obtained as dry powder after removing excess trifluoroacetic acid and water at 65 °C. Sodium trifluoroacetate (2 mmol) was added to the lutetium trifluoroacetate precursor along with oleic acid (6 mL),

oleylamine (6 mL), and 1-octadecene (12 mL) and heated to 120 °C under vacuum for 30 min to get a clear solution. The solution was subsequently heated to 300 °C (~20 °C/min) under argon and vigorously stirred until the reaction mixture turned turbid. Once turbid the reaction was left for another 5 min and then cooled to room temperature. The nanocrystals were precipitated by addition of ethanol, collected by centrifugation (1900g, 5 min), washed with ethanol and dispersed in hexane. Cubic (α) $NaLuF_4$ (X mol% Nd^{3+}, X = 2, 10)-doped nanocrystals were synthesized as described for the undoped cubic $NaLuF_4$, using Lu_2O_3 and Nd_2O_3 in respective molar ratios. Cubic (α) $NaLuF_4$ (X mol% Yb^{3+}, X = 10, 20)-doped nanocrystals were synthesized as described for the undoped cubic $NaLuF_4$, using Lu_2O_3 and Yb_2O_3 in respective molar ratios.

Synthesis of Core−Shell Nanocrystals. Hexagonal phase (β) $NaYF_4$ (X mol% Er^{3+}) (X = 5, 25, 50, 100) core−$NaLuF_4$ shell nanocrystals were synthesized following a previously reported method based on self-focusing by ripening.[24] To the core nanocrystals synthesized as described above, after 1 h at 300 °C, sacrificial nanocrystals (0.5 mmol, α-$NaLuF_4$) in 1-octadecene (1 mL) was injected and ripened for 12 min, followed by five more sacrificial nanocrystal injection (0.5 mmol each) and ripening cycle of 12 min each to yield core−shell NCs. After the final injection and ripening cycle (total ~3 mmol) the solution was cooled down to room temperature and the core−shell nanocrystals were precipitated by addition of ethanol, collected by centrifugation (1900g, 5 min), and washed with ethanol before dispersing them in chloroform (10 mL).

Hexagonal phase (β) $NaErF_4$ core−$NaLuF_4$ (X mol% Nd^{3+}, X = 2, 10)-doped shell nanocrystals were synthesized as described above using sacrificial (α-$NaLuF_4$:X mol% Nd^{3+}-doped, X = 2, 10) nanocrystals were used as shell precursors. Hexagonal phase (β) $NaErF_4$ core−$NaLuF_4$ (X mol% Yb^{3+}, X = 10, 20)-doped shell nanocrystals were synthesized as described above except that, sacrificial (α-$NaLuF_4$:X mol% Yb^{3+}-doped, X = 10, 20) nanocrystals were used as shell precursors.

Hexagonal phase (β) $NaErF_4$ core−$NaLuF_4$ shell nanocrystals with variable shell thickness were synthesized as described above for

NaErF$_4$ core–NaLuF$_4$ shell nanocrystals. To the core nanocrystals synthesized as described above, after 1 h at 300 °C, aliquot of the reaction mixture (1 mL) was retrieved as core nanocrystals and sacrificial (0.5 mmol, α-NaLuF$_4$) in 1-octadecene (1 mL) was injected and ripened for 12 min, followed by five more sacrificial nanocrystal injection (0.5 mmol each) and ripening cycles of 12 min each to yield core–shell NCs. Core–shell nanocrystals with variable shell thickness were obtained by removing reaction mixture (1 mL) after every two injection and ripening cycles, totaling an injection of ~1 mmol of shell sacrificial nanocrystals for every shell thickness. After the final injection and ripening cycle (total ~3 mmol) the solution was cooled down to room temperature and the core–shell nanocrystals were precipitated by addition of ethanol, collected by centrifugation (1900g, 5 min), and washed with ethanol before dispersing them in chloroform (10 mL). The obtained reaction aliquots with core and core–shell nanocrystals with variable shell thickness were purified as described above and dispersed in chloroform (1 mL).

Characterization. Hexane dispersions of the nanocrystals were drop-cast on a carbon-coated (400 mesh Cu) grid and air-dried before imaging. Size and size distribution analysis from the TEM images were obtained by measuring approximately 50 crystals. High-resolution transmission electron microscopy (HR-TEM) images were obtained from a FEI Sphera microscope operating at 120 kV. Scanning electron microscopy (SEM) images were obtained from a FEI SFEG-UHR (ultrahigh resolution) microscope. Hexane dispersions of the nanocrystals were drop-cast on a silicon wafer and dried under vacuum before imaging. Powder X-ray diffraction (XRD) patterns were collected using a Bruker D8 Advance instrument equipped with a 1-D Lynxeye silicon strip detector and Cu radiation (Kα radiation, λ = 1.54178 Å) using a step size of 0.02° and scan rate of 0.25 s per step. The sample was spun during collection to limit preferred orientation peaks. Upconversion emission spectra were obtained using a Fluorolog modular spectrofluorometer (Horiba) coupled with a 980 or 800 nm continuous-wave diode laser (Thorlabs) at an irradiance of 50–60 W cm^{-2}. Absolute upconversion quantum yield was obtained using a Horiba Jobin Yvon Fluorolog-3 spectrometer and a calibrated integrating sphere using a 980 nm CW diode laser operating at 10 W cm^{-2}. A neutral density filter on the excitation side (Thorlabs, NDUV10A, OD = 1.0) was used, along with a short-pass filter on the emission end (Semrock, FF01-750/SP-25). The colloidal nanocrystal dispersion in toluene and solvent alone as blank were taken in a cylindrical quartz cuvette and used for determining the upconversion quantum yield. Emission spectra of the nanocrystal dispersion and the blank solvent were collected at 10 W cm^{-2} between 500 and 750 nm, along with the spectra of the scattered excitation light (970–990 nm), and corrected for detector sensitivity. The absolute quantum yield (QY) of the sample was determined from the integrated intensity of the emission (em) and scattering (ex) spectrum, calculated as QY = $(I_{em,NCs} - I_{em,blank})/(I_{ex,blank} - I_{ex,NCs})$. Average QY was obtained from five successive measurements, where one measurement refers to the sample emission spectra, and then collecting the sample scattered excitation light spectra, followed by replacing the sample with the solvent blank reference and collecting the excitation light spectra scattered by the solvent followed by emission spectra of the blank. The absolute QY for these each measurement was determined as described above and averaged. Lifetime measurements was obtained from Edinburgh FLS980 spectrometer with single monochromators and multichannel scaling (MCS) mode. The maximum pulse duration was 360 μs. The excitation laser for 800 nm was a CNI laser (MLL-H-800-2.5W), and for 980 nm was a CNI laser (MLL-III-980-2W). On the emission end, a short-pass filter was used (Semrock, FF01-750/SP-25), and an excitation single-band bandpass filter for the 800 nm laser (FF01-794/32-25). Average excited state lifetimes were determined from biexponential fits and calculated using $\tau_{avg} = (A_1\tau_1^2 + A_2\tau_2^2)/(A_1\tau_1 + A_2\tau_2)$. Emission spectra of the downshifted emission in the NIR spectral region was collected with an Acton SP2300i spectrometer equipped with an InGaAs linear array detector (Princeton OMA-V) and using an 808 or 658 nm laser excitation. NIR fluorescence images of the downshifted emission were obtained using 2D InGaAs array

(Princeton Instruments) with 350×256 pixel using 808 or 658 nm laser excitation at 1 or 5 ms exposure, respectively.

■ ASSOCIATED CONTENT

ⓢ Supporting Information

The Supporting Information is available free of charge on the ACS Publications website at DOI: 10.1021/jacs.7b00223.

Complete details of synthesis, and characterization data, including Figures S1–S10 (PDF)

■ AUTHOR INFORMATION

Corresponding Author
*aalmutairi@ucsd.edu

ORCID
Noah J. J. Johnson: 0000-0002-0721-3186
Adah Almutairi: 0000-0001-5339-0207

Author Contributions
[⊥]N.J.J. and S.H. contributed equally.

Notes
The authors declare no competing financial interest.

■ ACKNOWLEDGMENTS

■ REFERENCES

(1) Wang, F.; Han, Y.; Lim, C. S.; Lu, Y.; Wang, J.; Xu, J.; Chen, H.; Zhang, C.; Hong, M.; Liu, X. *Nature* **2010**, *463*, 1061−1065.
(2) Wu, S.; Han, G.; Milliron, D. J.; Aloni, S.; Altoe, V.; Talapin, D. V.; Cohen, B. E.; Schuck, P. J. *Proc. Natl. Acad. Sci. U. S. A.* **2009**, *106*, 10917−10921.
(3) Su, L. T.; Karuturi, S. K.; Luo, J.; Liu, L.; Liu, X.; Guo, J.; Sum, T. C.; Deng, R.; Fan, H. J.; Liu, X.; Tok, A. I. Y. *Adv. Mater.* **2013**, *25*, 1603−1607.
(4) Goldschmidt, J. C.; Fischer, S. *Adv. Opt. Mater.* **2015**, *3*, 510−535.
(5) Haase, M.; Schäfer, H. *Angew. Chem., Int. Ed.* **2011**, *50*, 5808−5829.
(6) Wegh, R. T.; Donker, H.; Oskam, K. D.; Meijerink, A. *Science* **1999**, *283*, 663−666.
(7) Auzel, F. *Chem. Rev.* **2004**, *104*, 139−173.
(8) Dong, H.; Sun, L.-D.; Yan, C.-H. *Chem. Soc. Rev.* **2015**, *44*, 1608−1634.
(9) Huang, X.; Han, S.; Huang, W.; Liu, X. *Chem. Soc. Rev.* **2013**, *42*, 173−201.
(10) Ye, X.; Collins, J. E.; Kang, Y.; Chen, J.; Chen, D. T. N.; Yodh, A. G.; Murray, C. B. *Proc. Natl. Acad. Sci. U. S. A.* **2010**, *107*, 22430−22435.
(11) Chan, E. M.; Levy, E. S.; Cohen, B. E. *Adv. Mater.* **2015**, *27*, 5753−5761.
(12) Stouwdam, J. W.; van Veggel, F. C. J. M. *Nano Lett.* **2002**, *2*, 733−737.
(13) Zhang, Y.; Liu, X. *Nat. Nanotechnol.* **2013**, *8*, 702−703.
(14) Zhao, J.; Jin, D.; Schartner, E. P.; Lu, Y.; Liu, Y.; Zvyagin, A. V.; Zhang, L.; Dawes, J. M.; Xi, P.; Piper, J. A.; Goldys, E. M.; Monro, T. M. *Nat. Nanotechnol.* **2013**, *8*, 729−734.

(15) Gargas, D. J.; Chan, E. M.; Ostrowski, A. D.; Aloni, S.; Altoe, M. V. P.; Barnard, E. S.; Sanii, B.; Urban, J. J.; Milliron, D. J.; Cohen, B. E.; Schuck, P. J. *Nat. Nanotechnol.* **2014**, *9*, 300−305.

(16) Wang, J.; Deng, R.; MacDonald, M. A.; Chen, B.; Yuan, J.; Wang, F.; Chi, D.; Andy Hor, T. S.; Zhang, P.; Liu, G.; Han, Y.; Liu, X. *Nat. Mater.* **2014**, *13*, 157−162.

(17) Wei, W.; Chen, G.; Baev, A.; He, G. S.; Shao, W.; Damasco, J.; Prasad, P. N. *J. Am. Chem. Soc.* **2016**, *138*, 15130−15133.

(18) Tu, L.; Liu, X.; Wu, F.; Zhang, H. *Chem. Soc. Rev.* **2015**, *44*, 1331−1345.

(19) Chen, X.; Peng, D.; Ju, Q.; Wang, F. *Chem. Soc. Rev.* **2015**, *44*, 1318−1330.

(20) Johnson, N. J. J.; van Veggel, F. C. J. M. *Nano Res.* **2013**, *6*, 547−561.

(21) Chen, G.; Agren, H.; Ohulchanskyy, T. Y.; Prasad, P. N. *Chem. Soc. Rev.* **2015**, *44*, 1680−1713.

(22) Wang, F.; Wang, J. A.; Liu, X. G. *Angew. Chem., Int. Ed.* **2010**, *49*, 7456−7460.

(23) Zhang, F.; Che, R. C.; Li, X. M.; Yao, C.; Yang, J. P.; Shen, D. K.; Hu, P.; Li, W.; Zhao, D. Y. *Nano Lett.* **2012**, *12*, 2852−2858.

(24) Johnson, N. J. J.; Korinek, A.; Dong, C.; van Veggel, F. C. J. M. *J. Am. Chem. Soc.* **2012**, *134*, 11068−11071.

(25) Su, Q.; Han, S.; Xie, X.; Zhu, H.; Chen, H.; Chen, C.-K.; Liu, R.-S.; Chen, X.; Wang, F.; Liu, X. *J. Am. Chem. Soc.* **2012**, *134*, 20849−20857.

(26) Wang, F.; Deng, R. R.; Wang, J.; Wang, Q. X.; Han, Y.; Zhu, H. M.; Chen, X. Y.; Liu, X. G. *Nat. Mater.* **2011**, *10*, 968−973.

(27) Liu, Y. S.; Tu, D. T.; Zhu, H. M.; Li, R. F.; Luo, W. Q.; Chen, X. Y. *Adv. Mater.* **2010**, *22*, 3266−3271.

(28) Deng, R.; Qin, F.; Chen, R.; Huang, W.; Hong, M.; Liu, X. *Nat. Nanotechnol.* **2015**, *10*, 237−242.

(29) Wen, H. L.; Zhu, H.; Chen, X.; Hung, T. F.; Wang, B. L.; Zhu, G. Y.; Yu, S. F.; Wang, F. *Angew. Chem., Int. Ed.* **2013**, *52*, 13419−13423.

(30) Xie, X. J.; Gao, N. Y.; Deng, R. R.; Sun, Q.; Xu, Q. H.; Liu, X. G. *J. Am. Chem. Soc.* **2013**, *135*, 12608−12611.

(31) Chen, X.; Jin, L.; Kong, W.; Sun, T.; Zhang, W.; Liu, X.; Fan, J.; Yu, S. F.; Wang, F. *Nat. Commun.* **2016**, *7*, 10304.

(32) Li, Z. Q.; Zhang, Y.; Jiang, S. *Adv. Mater.* **2008**, *20*, 4765−4769.

(33) Johnson, N. J. J.; van Veggel, F. C. J. M. *ACS Nano* **2014**, *8*, 10517−10527.

(34) Capobianco, J. A.; Vetrone, F.; Boyer, J. C.; Speghini, A.; Bettinelli, M. *J. Phys. Chem. B* **2002**, *106*, 1181−1187.

(35) Wang, Y. F.; Liu, G. Y.; Sun, L. D.; Xiao, J. W.; Zhou, J. C.; Yan, C. H. *ACS Nano* **2013**, *7*, 7200−7206.

(36) Naczynski, D. J.; Tan, M. C.; Zevon, M.; Wall, B.; Kohl, J.; Kulesa, A.; Chen, S.; Roth, C. M.; Riman, R. E.; Moghe, P. V. *Nat. Commun.* **2013**, *4*, 2199.

(37) Hong, G.; Diao, S.; Chang, J.; Antaris, A. L.; Chen, C.; Zhang, B.; Zhao, S.; Atochin, D. N.; Huang, P. L.; Andreasson, K. I.; Kuo, C. J.; Dai, H. *Nat. Photonics* **2014**, *8*, 723−730.

(38) Hong, G.; Zou, Y.; Antaris, A. L.; Diao, S.; Wu, D.; Cheng, K.; Zhang, X.; Chen, C.; Liu, B.; He, Y.; Wu, J. Z.; Yuan, J.; Zhang, B.; Tao, Z.; Fukunaga, C.; Dai, H. *Nat. Commun.* **2014**, *5*, 4206.

(39) Polman, A. *J. Appl. Phys.* **1997**, *82*, 1−39.

(40) Miritello, M.; Cardile, P.; Lo Savio, R.; Priolo, F. *Opt. Express* **2011**, *19*, 20761−20772.

(41) Vetrone, F.; Naccache, R.; Mahalingam, V.; Morgan, C. G.; Capobianco, J. A. *Adv. Funct. Mater.* **2009**, *19* (18), 2924−2929.